



**HAL**  
open science

## Sentinel-2 image capacities to predict common topsoil properties of temperate and Mediterranean agroecosystems

Emmanuelle Vaudour, Cécile Gomez, Youssef Fouad, Philippe Lagacherie

► **To cite this version:**

Emmanuelle Vaudour, Cécile Gomez, Youssef Fouad, Philippe Lagacherie. Sentinel-2 image capacities to predict common topsoil properties of temperate and Mediterranean agroecosystems. *Remote Sensing of Environment*, 2019, 223, pp.21-33. 10.1016/j.rse.2019.01.006 . hal-01990153

**HAL Id: hal-01990153**

**<https://hal.science/hal-01990153>**

Submitted on 21 Oct 2021

**HAL** is a multi-disciplinary open access archive for the deposit and dissemination of scientific research documents, whether they are published or not. The documents may come from teaching and research institutions in France or abroad, or from public or private research centers.

L'archive ouverte pluridisciplinaire **HAL**, est destinée au dépôt et à la diffusion de documents scientifiques de niveau recherche, publiés ou non, émanant des établissements d'enseignement et de recherche français ou étrangers, des laboratoires publics ou privés.



Distributed under a Creative Commons Attribution - NonCommercial 4.0 International License

1 **SENTINEL-2 image capacities to predict common topsoil properties of temperate and**  
2 **Mediterranean agroecosystems**

3

4 E. Vaudour<sup>1\*</sup>, C. Gomez<sup>2</sup>, Y. Fouad<sup>3</sup>, P. Lagacherie<sup>4</sup>

5

6 <sup>1</sup>UMR ECOSYS, AgroParisTech, INRA, Université Paris-Saclay, 78850, Thiverval-Grignon,  
7 France \*Email: Emmanuelle.Vaudour@agroparistech.fr

8 <sup>2</sup>IRD, UMR LISAH (INRA-IRD-SupAgro), F-34060 Montpellier, France

9 <sup>3</sup>UMR SAS, Agrocampus Ouest, INRA, 35042, Rennes, France

10 <sup>4</sup>INRA, UMR LISAH (INRA-IRD-SupAgro), F-34060 Montpellier, France

11

12

13 **Abstract**

14 To be fully operational for facilitating decisions made at any spatial level, models and  
15 indicators of soil ecosystem functions require the use of precise spatially referenced soil  
16 information as inputs. This study aimed at exploring the capacity for SENTINEL-2A (S2A)  
17 multispectral satellite images to predict several topsoil properties in two contrasted  
18 pedoclimatic environments: a temperate region marked by intensive annual crop cultivation  
19 patterns and soils derived from loess or colluvium and/or marine limestone or chalk  
20 (Versailles Plain, 221 km<sup>2</sup>); and a Mediterranean region marked by vineyard cultivation and  
21 soils derived from lacustrine limestone, calcareous sandstones, colluvium, or alluvial deposits  
22 (Peyne catchment, 48 km<sup>2</sup>). Prediction models of soil properties based on partial least squares  
23 regressions (PLSR) were built from S2A spectra of 72 and 143 sampling locations across the  
24 Versailles Plain and Payne catchment, respectively. Eight soil surface properties were  
25 investigated in both regions: pH, cation exchange capacity (CEC), texture fractions (Clay,

26 Silt, Sand), Iron, Calcium Carbonate ( $\text{CaCO}_3$ ) and Soil Organic Carbon (SOC) content.  
27 Predictive abilities were studied according to the root mean square error of cross-validation  
28 (RMSECV) tests, cross-validated coefficient of determination ( $R^2_{cv}$ ) and ratio of performance  
29 to deviation (RPD). Intermediate prediction performance outcomes ( $R^2_{cv}$  and RPD greater  
30 than or equal to 0.5 and 1.4, respectively) were obtained for 4 topsoil properties found across  
31 the Versailles Plain (SOC, pH,  $\text{CaCO}_3$  and CEC), and near-intermediate performance  
32 outcomes ( $0.5 > R^2_{cv} > 0.39$ ,  $1.4 > \text{RPD} > 1.3$ ) were yielded for 3 topsoil properties (Clay,  
33 Iron, and CEC) found across the Payne catchment and for 1 property (Clay) found across the  
34 Versailles Plain. The study results show what can be expected from SENTINEL2 images in  
35 terms of predictive capacities at the regional scale. The spatial structure of the estimated soil  
36 properties for bare soils pixels is highlighted, promising further improvements made to spatial  
37 prediction models for these properties based on the use of Digital Soil Mapping (DSM)  
38 techniques.

39

40 Key words: soil properties, SENTINEL-2A, partial least squares regression, temperate soils,  
41 Mediterranean soils, agroecosystems.

42

### 43 **1. Introduction**

44 Soils carry out a number of key environmental functions that are essential for human  
45 subsistence (e.g., food, fiber and timber production, water storage and redistribution, pollutant  
46 filtering and carbon storage). The understanding and modeling of physical, chemical and  
47 biological processes underlying these different functions have been the subject of many  
48 scientific works now that a number of models or indicators that represent these functions are  
49 available (Sanchez et al., 2009; Adhikari and Hartemink, 2016; Baveye et al. 2016). To be  
50 fully operational in facilitating decisions made at local, national and global levels, these

51 models and indicators require the use of precise spatially referenced soil information as  
52 inputs.

53         Given the lack of precision and extension of existing soil databases, Digital Soil  
54 Mapping (Mc Bratney et al., 2003) methods have been recognized as the most adequate and  
55 operational response to these requirements (Arrouays et al., 2014, Minasny & McBratney,  
56 2016). However, even though digital soil maps of soil properties are now being produced  
57 across the globe (Arrouays et al., 2017) and for large areas—regions, countries and even  
58 continents—at high resolutions (100 m), they still provide very uncertain estimations of soil  
59 properties due to the limited availability of sites offering soil property measurements used for  
60 calibrating DSM models (Vaysse et al., 2015).

61         Visible, Near-infrared and Short-wave Infrared (VNIR/SWIR) hyperspectral remote  
62 sensing methods have been demonstrated to serve as promising means to significantly  
63 increase the number of sites offering quantitative estimations of topsoil properties (e.g., Soil  
64 Organic Carbon (SOC), pH, Cation Exchange Capacity (CEC), texture fractions (clay, silt,  
65 sand), Iron and Calcium Carbonate ( $\text{CaCO}_3$ )) (e.g., Selige et al., 2008; Stevens et al., 2010;  
66 Gomez et al., 2012; Vaudour et al., 2016). For bare soil surfaces, accurate local estimates  
67 ( $R^2_{cv} > 0.7$ ) have been obtained for soil properties i) related to a chemical species that impacts  
68 soil surface reflectance values through absorption bands (e.g., OH<sup>-</sup> ion for clay) (Ben-Dor et  
69 al., 2002) or ii) highly correlated with the latter (e.g., CEC with clay content) (Ben-Dor et al.,  
70 2002), iii) showing a sufficient level of variability across study regions (Gomez et al., 2012a  
71 & b). For instance, Selige et al. (2006) mapped SOC content, a soil property having specific  
72 spectral behaviour and high spatial variability over their study area. In addition, they also  
73 mapped Total Nitrogen, a soil property deprived of specific spectral features but, due to an  
74 associated chemical or physical structure, correlated to a soil property having such features  
75 (being SOC). DSM approaches are designed to employ this new source of soil data to allow

76 for the exhaustive mapping of surface (Walker et al., 2017) and subsurface (Lagacherie et al.,  
77 2013) properties.

78         Although hyperspectral VNIR/SWIR imagery has been proven to serve as a valuable  
79 tool for mapping key soil surface properties, it cannot be applied for large surface mapping or  
80 for temporal monitoring because it is expensive to apply and because hyperspectral  
81 VNIR/SWIR imaging data are not widely available. Indeed, only one hyperspectral  
82 VNIR/SWIR satellite sensor is currently operational. The HYPERION sensor offers a spatial  
83 resolution of 30 m, a spectral resolution of 10 nm and a swath of 7.5 km (Folkman et al.,  
84 2001). Other hyperspectral VNIR/SWIR imaging sensors are airborne sensors (e.g., the  
85 Hymap, AISA-DUAL and HySpex sensors) with spectral resolutions of 5 to 10 nm, spatial  
86 resolutions of approximately 4-5 m (depending to the flight altitude) and flight prints of  
87 generally less than 400 km<sup>2</sup> (depending to the studied case). Furthermore, few studies have  
88 obtained successful results in terms of mapping soil properties from VNIR-SWIR  
89 multispectral satellite imagery that allow one to capture a larger area from a single nearly  
90 instantaneous glance (e.g., Vaudour et al., 2013; Shabou et al., 2015). This can be attributed  
91 to i) the low revisit frequency of sensors, which compromises the acquisition of images under  
92 clear conditions, while time ranges of bare soil availability, and particularly for annual crop  
93 systems, are short and ii) the coarse spectral and spatial resolutions of most historical  
94 multispectral sensors, which limit prediction performance outcomes (Gomez et al, 2015;  
95 Adeline et al., 2017).

96         The recent release of multispectral satellite SENTINEL-2A data by the European  
97 Space Agency last November 2015 is revolutionary in developing images of large areas with  
98 a 290 km-swath width at high revisit frequencies (planned to be near-daily when the full  
99 satellite constellation is in orbit). The multispectral SENTINEL-2A satellite provides 13

100 spectral bands at spectral resolutions of between 20 and 180 nm and at spatial resolutions of  
101 10 to 60 m (§2.3).

102 The objective of this study is to assess the potential for SENTINEL-2A data to  
103 produce estimations of topsoil properties for large sets of sites. The study focuses on two  
104 French regions—the Versailles Plain and the Peyne Valley—that represent very different  
105 agroecosystems and that have both been previously used as test areas for topsoil mapping  
106 from VNIR/SWIR hyperspectral data (Vaudour et al, 2016 and Gomez et al, 2012,  
107 respectively).

108

109

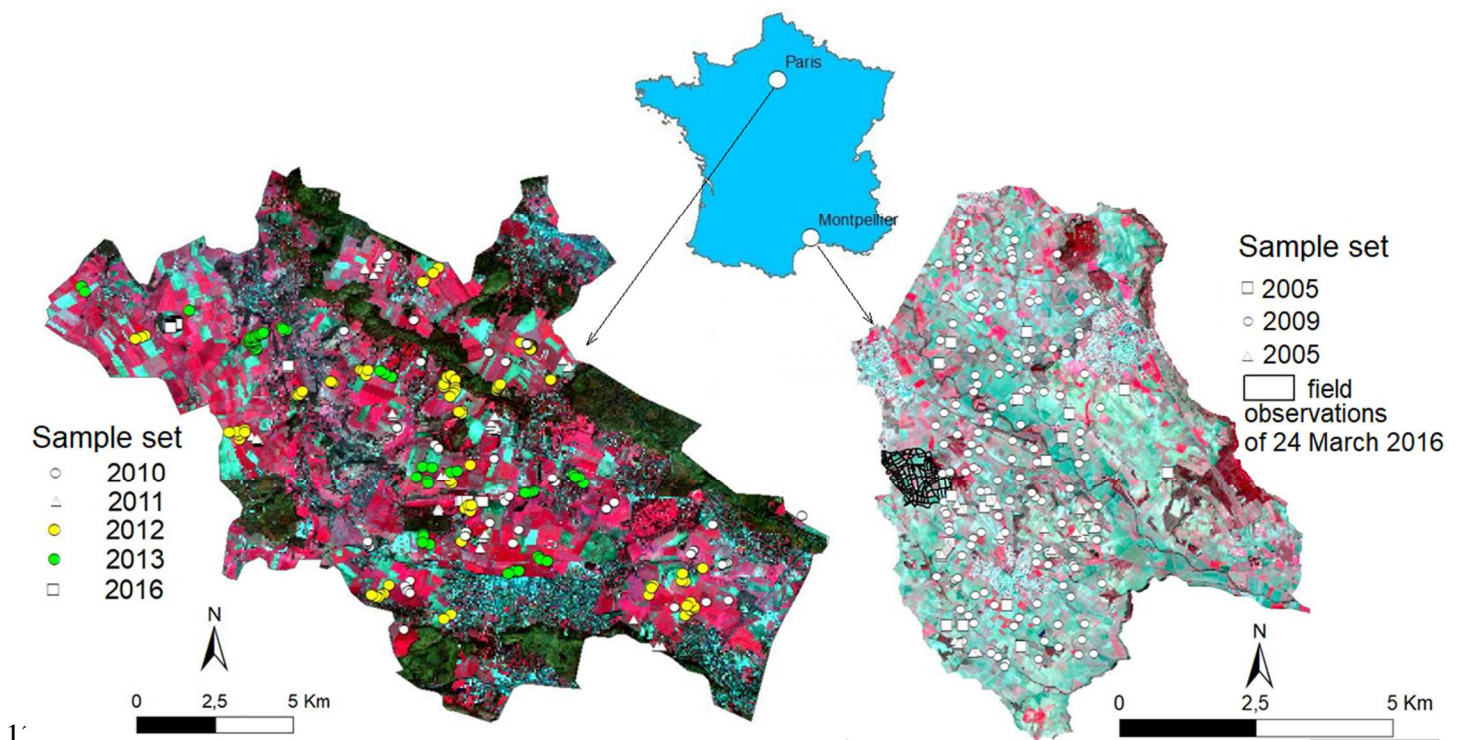
## 110 **2. Materials**

### 111 *2.1 Study areas*

#### 112 2.1.1 Versailles Plain

113 The Versailles Plain is an agricultural peri-urban region of 221 km<sup>2</sup> located west of Paris  
114 (North of France) that is characterized by intensive annual crop cultivation across an area of  
115 ~99 km<sup>2</sup> (Fig. 1, left). The main crop rotations in the area involve winter wheat, winter  
116 rapeseed, winter and spring barley and maize on occasion (Vaudour et al., 2015). Cultivation  
117 practices are mainly conventional, with early winter plowing applied at least 1 year out of  
118 every 3. The Versailles Plain is composed of two plateaus levels: one at a 120-m elevation in  
119 the center (lower limestone plateau) and another at a 170 m-elevation along the northern and  
120 southern edges of the area (upper millstone clay plateau). Both are oriented in the NW-SE  
121 direction toward the Palace of Versailles. Quaternary loessic deposits and loessic colluvium  
122 leave a mark on all landforms in the area and particularly on local plateaus, which have  
123 evolved into haplic or glossic luvisols according to the FAO classification (World Reference  
124 Base (WRB) (Crahet, 1992; Vaudour et al., 2013, 2014). The largely forested upper plateau

125 flanks are characterized by Fontainebleau acid sands that give rise to arenic cambisols, while  
 126 the lower plateau flanks, which are largely cultivated, are composed of calcaric cambisols  
 127 derived from limestone, colluvial materials and, along the lower slopes, chalk. Throughout the  
 128 lower slopes and valleys, stagnic colluvic cambisols are derived from marls or alluvio-  
 129 colluvial materials.  
 130



131  
 132 Figure 1. Locations of soil samples from the Versailles Plain (left, infrared colored S2A  
 133 image from 12 March 2016) and the lower Peyne Valley (right, infrared colored S2A image  
 134 from 19 March 2016), ©ESA 2016

135  
 136 2.1.2 La Peyne Valley

137 The lower valley of the Peyne River is a viticultural region of 48 km<sup>2</sup> located west of  
 138 Montpellier (South of France) (Fig. 1, right) and characterized by Plio-Quaternary alluvial  
 139 terraces and fan terraces, the deposits of which have undergone fersiallitization and which

140 have evolved into red Mediterranean soils or chromic luvisols (Coulouma, 2008). The valley  
141 base has been composed of marine Miocene sediments (marl, sandy loam, and calcareous  
142 sandstone) and marine Pliocene marl refillings since the Messinian salinity crisis. Gently  
143 undulating forms of hills and colluvial fans characterize landscape units in the area and give  
144 rise to several types of soils rich in calcium carbonate with a loamy sand texture and  
145 increasing clay levels toward the bases of the hillslopes: calcaric leptosols, calcaric regosols,  
146 and calcisols. A cuesta that characterizes the landscape unit has formed on lacustrine  
147 limestone of the Upper Miocene, where calcisols and calcaric regosols have developed with  
148 irregular bedrock depths creating variations in stoniness and calcium carbonate content levels.  
149 Alluvial terraces and alluvio-colluvial fans originating from Plio-Quaternary clays and  
150 alluvial deposits correspond to deep stony decarbonated chromic and/or colluvial luvisols,  
151 fluvisols, and some endogleyic calcisols. While early Quaternary terraces of the Peyne River  
152 have produced stony and clayey chromic luvisols, newer terraces have balanced textured  
153 fluvisols with carbonate content.

154

## 155 *2.2 Soil samples and ground observations*

### 156 *2.2.1 Soil sampling*

157 This study gathered two soil data sets that were collected for the purpose of earlier studies (for  
158 Versailles, Vaudour et al. 2013, 2014a, 2016; for La Peyne, Gomez et al, 2012). Despite some  
159 differences in chemical analysis, it was found useful to gather them in view of enlarging the  
160 range of the tested pedological situations. A total of 72 and 143 topsoil samples were  
161 collected from the Versailles Plain and Peyne Valley, respectively (Fig. 1). For the Versailles  
162 Plain, 69 topsoil samples were collected from 2010 to 2013, and 13 topsoil samples were  
163 collected in 2016. All of the samples were composed of roughly 10 sub-samples collected to a  
164 depth of 8 cm from random locations within a  $2.7 \times 2.7$  m square area centered at the

165 sampling plot as recorded at its center using a Trimble Pathfinder®Power DGPS of 50 cm  
 166 precision (Vaudour et al., 2014). From the Peyne Valley, 39 topsoil samples were collected in  
 167 2005, and 104 topsoil samples were collected in 2009. All of the samples were composed of  
 168 five sub-samples collected to a depth of 5 cm from random locations within a 10 × 10 m  
 169 square centered on the geographical position of the sampling plot as recorded by a Garmin  
 170 GPS instrument.

171

172

### 173 2.2.2 Physico-chemical analysis

174 Topsoil samples collected from both study areas were air-dried and then crushed and sieved to  
 175 2 mm. Soil property determinations were performed through a classical physico-chemical  
 176 analysis (Baize and Jabiol, 1995). In total, 8 common soil properties were considered for  
 177 spectral modeling (Table 1): content of 3 particle sizes or granulometric fractions of 2 mm-  
 178 sieved fine earth (total silt, 2 - 50 µm; total sand, 50 µm - 2 mm and clay, < 2 µm); calcium  
 179 carbonate (CaCO<sub>3</sub>) content; free iron content (Mehra-Jackson); soil organic carbon (SOC)  
 180 content; pH; and cation exchange capacity (CEC).

181 Granulometric fractions (clay, silt, and sand) and CaCO<sub>3</sub> content levels were measured  
 182 from 143 soils samples collected from the Peyne Valley (Table 1). The three other soil  
 183 properties (iron, CEC and pH) were measured from 104 soil samples collected from the Peyne  
 184 Valley. For the Versailles Plain, all soil properties except for CEC (39 samples) were  
 185 measured (Table 1).

186

187 Table 1. Soil datasets used for models and statistics on soil properties

Soil property	Description	Unit	Versailles Plain					Peyne Valley						
			Sample size	Min	Q1	Median	Q3	Max	Sample size	Min	Q1	Median	Q3	Max
SOC	soil organic C	g.kg <sup>-1</sup>	72	7.0	12.5	15.9	20.1	31.9	104	4.0	7.0	8.9	11.4	21.8

CaCO <sub>3</sub>	content total CaCO <sub>3</sub>	g.kg <sup>-1</sup>	72	0	0	27.1	67.2	530	143	0	22.2	136.0	251.0	473
Clay	content granulometric fraction <2 µm	g.kg <sup>-1</sup>	72	132	192.5	249.5	281.0	391	143	67	185.0	231.0	290.5	452
Silt	granulometric fraction 2-50 µm	g.kg <sup>-1</sup>	72	228	474.8	542.0	603.0	774	143	141	252.0	322.0	384.5	655
Sand	granulometric fraction 50 µm – 2 mm	g.kg <sup>-1</sup>	72	17	87.8	157.5	209.0	512	143	106	364.5	433.0	516.0	737
Iron	« free iron » content	g/100 g	72	0.51	0.75	0.87	0.97	1.29	104	0.03	0.75	1.07	1.58	2.92
pH	water-pH	-	72	5.61	6.91	7.99	8.18	8.34	104	5.37	8.3	8.46	8.54	8.70
CEC	cation exchange capacity	cmol.kg <sup>-1</sup>	39	6.1	11.0	17.1	22.1	28.3	104	6.1	8.3	10.7	12.9	19.1

188

189

### 190 2.2.3 Ground observations

191 For the Versailles Plain, soil surface conditions were observed on 15 and 17 March 2016  
 192 across 6 agricultural fields and for other fields planned for spectral measurements. For the  
 193 Peyne Valley, vineyard soil surface conditions were observed on 24 March 2016 across the  
 194 0.9 km<sup>2</sup> sub-catchment of Roujan, which includes 75 viticultural fields. These observations  
 195 enabled us to define the threshold of the vegetation index for retrieving bare soil pixels from  
 196 S2A images. At the time that the images were acquired, the budburst stage had just begun for  
 197 vines in the Peyne Valley, and hence vine vegetation had not yet developed. For the  
 198 Versailles Plain, spring barley sowing had just started and maize and pea sowing had not  
 199 started, hence allowing for the observation of bare soils used for spring crops. For both study  
 200 areas, winter crops and grasslands were photosynthetically active and covering, and thus  
 201 easily identifiable and removable by means of NDVI.

202

### 203 2.3 Remotely sensed images and geographic data

204 Two SENTINEL-2A (S2A) images were acquired under nearly clear conditions on 12 and 19  
 205 March 2016 from the Versailles Plain and Peyne Valley, respectively (Table 2). The

206 multispectral instrument aboard the S2A satellite has 13 spectral bands, including 4 bands of a  
 207 10 m resolution and 6 bands of a 20 m resolution (Table 3) retained for spectral modeling.  
 208 Both images were atmospherically corrected using the ATCOR2/3 radiative transfer model  
 209 (Richter and Schläpfer, 2016).

210 Both study sites are characterized by urban activity and by the presence of bare soil,  
 211 water and vegetation. To mask no-soil pixels from the S2 data, the following approach was  
 212 applied. First, urban and water areas were masked using Land Parcel Registry maps. In turn,  
 213 only cropland and vineyards were maintained across the study areas. Second, pixels with  
 214 normalized difference vegetation index (NDVI) values exceeding an expert-calibrated  
 215 threshold were masked. A value of 0.35 was determined for both sites after considering field  
 216 observations (section 2.2.3). The NDVI was retrieved using bands of 842 nm and 665 nm.  
 217 Finally, bare soils of the Versailles Plain represent 8.05% of our study area and 44,979 S2A  
 218 pixels, while bare soils of the Payne catchment represent 38.6% of our study area and 46,971  
 219 S2A pixels.

220

221 Table 2. Main characteristics of the studied scenes

Imaging date	Sensor	Output resolution (m)	Time of acquisition (U.T GMT)	Viewing incidence angle (°)	Sun azimuth (°)	Sun elevation (°)
12 March 2016	S2A	20	10:50:37	<5.1	160.5	36.1
19 March 2016	S2A	20	10:40:32	<3.3	157.6	43.7

222

223 Table 3. Characteristics of the Multi-Spectral Instrument aboard the SENTINEL2 satellite.

224 Spectral S2A bands used are shown in bold.

Spectral band	Spatial resolution (m)	Central wavelength (nm)	Band width (nm)
b1	60	443	20
<b>b2</b>	<b>10</b>	<b>490</b>	<b>65</b>
<b>b3</b>	<b>10</b>	<b>560</b>	<b>35</b>
<b>b4</b>	<b>10</b>	<b>665</b>	<b>30</b>
<b>b5</b>	<b>20</b>	<b>705</b>	<b>15</b>
<b>b6</b>	<b>20</b>	<b>740</b>	<b>15</b>
<b>b7</b>	<b>20</b>	<b>783</b>	<b>20</b>
<b>b8</b>	<b>10</b>	<b>842</b>	<b>115</b>
<b>b8A</b>	<b>20</b>	<b>865</b>	<b>20</b>
b9	60	945	20

b10	60	1380	30
<b>b11</b>	<b>20</b>	<b>1610</b>	<b>90</b>
<b>b12</b>	<b>20</b>	<b>2190</b>	<b>180</b>

225

226

227

228

229

230

231

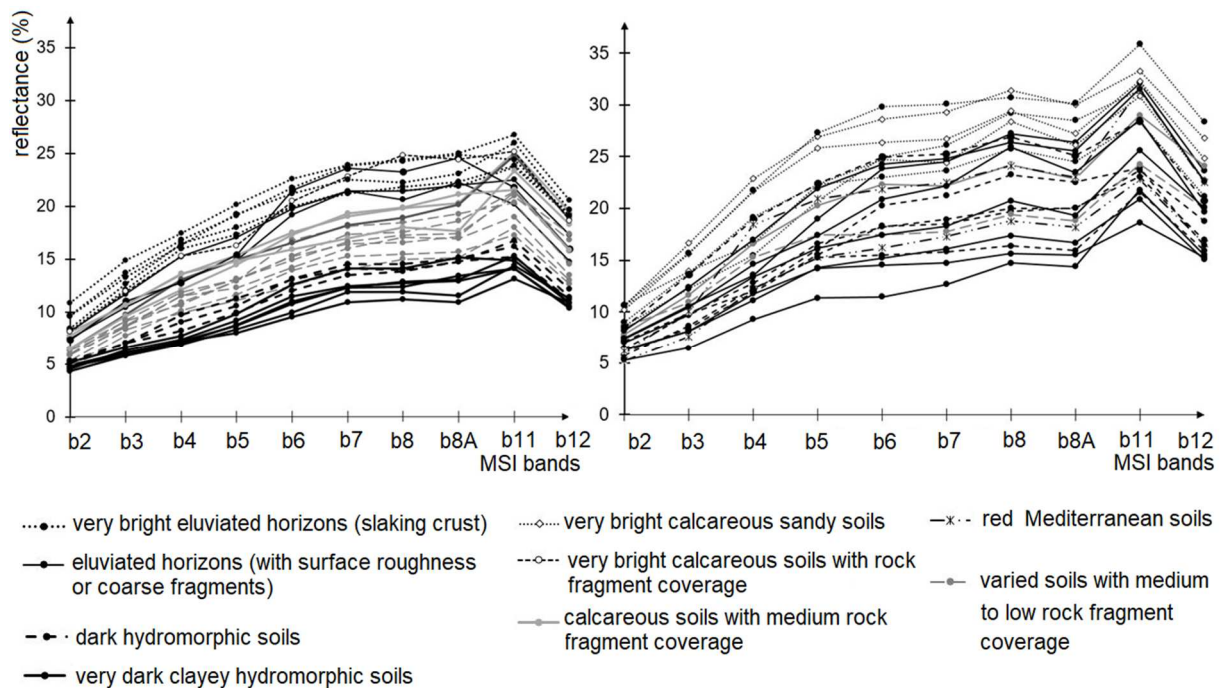
232

233

234

235

A selection of various reflectance spectra comprising the darkest and the brightest soils is shown in Fig. 2. The brightest soils comprise: (i) calcic or calcareous sandy soils originating from calcareous sandstone (La Peyne); (ii) silt-loam luvisols (Versailles) or eluviated horizons of the chromic luvisols (La Peyne), developing a slaking crust ; (iii) rendzic or calcareous cambisols with very high topsoil calcium carbonate content or outcropping underlying chalk (Versailles). The darkest soils are clayey and alluvial and, for Versailles, can have high organic carbon content (>20 g kg<sup>-1</sup>) and/or high roughness dating from late winter ploughing. Intermediate soil spectra comprise soils with either moderate rock fragment content (10–25%), or varied textures and intermediate to low roughness (both regions), and also red Mediterranean soils (La Peyne).



236

237

238

239

240

Figure 2. Selection of reflectance image spectra covering the whole dataset reflectance range and the main soil types

### 3. Methods

241 *3.1 Models for soil property prediction*

242 The partial least squares regression (PLSR) method was used to construct prediction models  
243 based on bare soil samples drawn from each study region. The PLSR method relates two data  
244 matrices, the matrix of explanatory variables X (here the soil spectra) and the matrix of  
245 dependent variables Y (here the soil properties), through a linear multivariate model, but it  
246 extends beyond traditional regression methods in that it also models the structures of X and Y  
247 (Geladi and Kowalski, 1986; Wold et al., 2001). For Y in particular, PLSR extracts  
248 orthogonal or latent predictor variables accounting for variation in the dependent variable.  
249 The PLSR approach enables one to analyze data based on several noisy collinear features  
250 (Wold et al., 2001), and it has been used widely for hyperspectral remote sensing (e.g., Selige  
251 et al., 2008; Stevens et al., 2010; Gomez et al., 2012; Vaudour et al., 2016).

252 Prior to PLSR modeling, in order to maximize the fitting of target values against spectra, a  
253 series of transforms were tested for either spectra or target values. Reflectance values of the  
254 whole spectra were centered. For the Versailles Plain, Clay, SOC and CaCO<sub>3</sub> content levels  
255 and CEC were log-transformed, while for both areas, the square root of iron content was used.  
256 For La Peyne, log-transform of target values was not retained, as it did not bring any  
257 improvement of the fitting. Outliers were detected for sets of image spectra or for sets of  
258 measured soil properties. This was based on the 5% threshold of the standardized  
259 Mahalanobis distance (Mark and Tunnel, 1985) and on the multivariate outlier detection  
260 approach elaborated by Filzmoser et al. (2005). Outliers selected through both approaches  
261 were retained as outliers.

262 For each target soil property Y, a PLSR model was constructed from preprocessed image  
263 spectra with 10 selected spectral bands (Table 3). The optimal number of latent variables was  
264 determined from the prediction residual error sum of squares (PRESS). Due to the limited  
265 number of bare soil samples available, and because this study was more focused on

266 comparing performance levels between regions than on carrying out external validation  
267 assessments, a leave-one-out cross-validation procedure was applied (Wold, 1978; Gomez et  
268 al., 2012). The quality of model fit was evaluated from the root mean squared error of cross-  
269 validation (RMSECV), from the coefficient of determination of cross-validation ( $R_{cv}^2$ ) and  
270 from the residual prediction deviation (RPD), i.e., the ratio between the standard deviation of  
271 the calibration dataset to the RMSECV. According to Chang et al. (2001) and Viscarra-Rossel  
272 et al. (2006), values of 1.4 to 1.8 denote models exhibiting moderate levels of predictive  
273 capacity; values of between 1 and 1.4 denote models exhibiting poor levels of predictive  
274 capacity, and values of  $<1$  denote very poor models that should not be used.

275 PLSR models were used through R version 3.2.1 (R Development Core Team, 2015)  
276 employing the “pls” package (Mevik and Wehrens, 2007).

277

### 278 *3.2 Variograms of predicted soil properties*

279 For the best predicted soil properties, PLSR models were applied to pixels of bare agricultural  
280 soil. The spatial structure of the predicted pixels was examined and compared with that of  
281 measured properties for the same locations. Spatial structures can be described from a  
282 variogram that relates the spatial dependence or semi-variance between points at a distance of  
283  $h$ , i.e., the average variance between any pair of sampling points (Goovaerts, 1997):

$$284 \gamma(h) = \frac{1}{2n} \sum_{i=1}^n \{p(x_i) - p(x_i + h)\}^2 \quad (1)$$

285 where  $\gamma(h)$  is the average semi-variance of the soil property,  $n$  is the number of pairs of  
286 sampling points,  $p$  is the value of the property  $P$ ,  $x$  is the coordinate of the point, and  $h$  is the  
287 distance between pairs or the lag value.

288 For each best predicted soil property, two empirical variograms were built from  
289 equation (1): the first was built from 143 or 104 values of the soil samples measured by  
290 physico-chemical analysis; the second was built from predicted values for the same locations.

291 Simple omnidirectional variograms were calculated, and following Gomez et al. (2012), the  
292 spherical or exponential model used was fitted through a weighted least squares procedure  
293 (Pebesma, 2004) using the R statistical software program and the Gstats package. The  
294 universality condition (no drift) was assumed.

295 For the Versailles Plain, it was not possible to obtain experimental variograms suitable  
296 for fitting a model due to the limited number of sites involved and the clustered sampling  
297 scheme employed. Variograms were therefore only examined for the Peyne Valley. To  
298 examine the robustness of spatial structures at the scale of the entire study region, variograms  
299 were calculated from all bare soil pixels.

300

## 301 **4. Results**

### 302 *4.1 Description of soils samples*

303 Basic statistics on all of the soil properties measured are shown in Table 2. For the Peyne  
304 Valley, the range of clay contents present is higher than that of the Versailles Plain, with the  
305 highest value recorded as 452 g.kg<sup>-1</sup>, though the 1<sup>st</sup> quartile and median values (185.0 and  
306 231.0 g.kg<sup>-1</sup>) are slightly lower than those for the Versailles Plain (192.5 and 249.5 g.kg<sup>-1</sup>),  
307 while the 3<sup>rd</sup> quartile is slightly higher (290.5 g.kg<sup>-1</sup>) than that for the Versailles Plain (281  
308 g.kg<sup>-1</sup>). SOC, silt and CEC levels are measured within a narrower and lower range for the  
309 Peyne Valley and with a much lower median (SOC, 8.92 g.kg<sup>-1</sup>; silt content, 322 g.kg<sup>-1</sup>; CEC,  
310 10.65 cmol+.kg<sup>-1</sup>) than that for the Versailles Plain (SOC, 15.9 g.kg<sup>-1</sup>; silt content, 542 g.kg<sup>-1</sup>;  
311 CEC, 17.10 cmol+.kg<sup>-1</sup>). Conversely, sand and calcium carbonate content levels are higher in  
312 the Peyne Valley, with a higher median (sand content, 433 g.kg<sup>-1</sup>; calcium carbonate content,  
313 136 g.kg<sup>-1</sup>) than that for the Versailles Plain (sand content, 157.5 g.kg<sup>-1</sup>; calcium carbonate  
314 content, 27 g.kg<sup>-1</sup>). Consequently, pH values are higher and less variable for the Peyne  
315 Valley, while soils of the Versailles Plain vary more in terms of pH levels. Red Mediterranean

316 soils resulting from geochemical weathering contain more free iron, and hence their presence  
 317 has induced a higher range of Fe content levels, with the 3<sup>rd</sup> quartile reaching a value of 1.58  
 318 g/100 g compared to a value of 0.97 g/100 g found for the Versailles Plain.

319 Moreover, coarse fragment content levels in topsoil can reach percentages of as high  
 320 as 20% and 30% for the 3<sup>rd</sup> quartile of the Versailles and Payne sets, respectively.

321

322

323

324

325 Table 4. Pearson correlation table of common soil properties for the Versailles Plain

Variables	Clay	Silt	Sand	CaCO <sub>3</sub>	SOC	Fe	pH	CEC
Clay	<b>1.00</b>							
Silt	-0.24	<b>1.00</b>						
Sand	<b>-0.34</b>	-0.27	<b>1.00</b>					
CaCO <sub>3</sub>	-0.02	<b>-0.70</b>	<b>-0.33</b>	<b>1.00</b>				
SOC	<b>0.53</b>	<b>-0.38</b>	<b>-0.44</b>	<b>0.46</b>	<b>1.00</b>			
Fe	<b>0.48</b>	0.24	0.03	<b>-0.52</b>	0.00	<b>1.00</b>		
pH	<b>0.46</b>	<b>-0.43</b>	<b>-0.50</b>	<b>0.60</b>	<b>0.66</b>	-0.25	<b>1.00</b>	
CEC	<b>0.77</b>	<b>-0.32</b>	<b>-0.52</b>	<b>0.33</b>	<b>0.82</b>	0.12	<b>0.77</b>	<b>1.00</b>

326 *Values in bold are different from 0 at a significance level of alpha=0.05*

327

328 Table 5. Pearson correlation table of common soil properties of the Payne Valley

Variables	Clay	Silt	Sand	CaCO <sub>3</sub>	SOC	Fe	pH	CEC
Clay	<b>1.00</b>							
Silt	-0.14	<b>1.00</b>						
Sand	<b>-0.54</b>	<b>-0.76</b>	<b>1.00</b>					
CaCO <sub>3</sub>	-0.08	<b>0.53</b>	<b>-0.40</b>	<b>1.00</b>				
SOC	<b>-0.19</b>	0.08	0.06	0.11	<b>1.00</b>			
Fe	<b>0.42</b>	<b>-0.26</b>	-0.06	<b>-0.50</b>	-0.11	<b>1.00</b>		
pH	0.02	<b>0.42</b>	<b>-0.37</b>	<b>0.52</b>	0.03	<b>-0.42</b>	<b>1.00</b>	
CEC	<b>0.89</b>	-0.16	<b>-0.45</b>	0.00	-0.02	0.16	0.14	<b>1.00</b>

329 *Values in bold are different from 0 at a significance level of alpha=0.05*

330

331 For the Versailles Plain, the highest correlations ( $|R| > 0.7$ ) were observed between CEC and  
332 SOC content levels, between CEC and clay levels, between CEC and pH levels and between  
333  $\text{CaCO}_3$  and silt levels (Table 4). Modest correlations ( $0.7 > |R| > 0.5$ ) were observed between  
334 pH and SOC levels, between pH and  $\text{CaCO}_3$  levels, between pH and sand levels, between Iron  
335 and  $\text{CaCO}_3$  levels and between SOC and clay levels (Table 4). For the Payne catchment, the  
336 highest correlations ( $|R| > 0.7$ ) were observed between CEC and clay levels and between sand  
337 and silt levels (Table 5). Modest correlations ( $0.7 > |R| > 0.5$ ) were observed between pH and  
338  $\text{CaCO}_3$  levels, between iron and  $\text{CaCO}_3$  levels, between sand and clay levels and between silt  
339 and  $\text{CaCO}_3$  levels (Table 5).

340

#### 341 *4.2 Performance of the prediction models*

342 A PLSR model was built from S2A spectra and from each observed soil property associated  
343 with the available soil samples. No spectral outliers were removed from the calibration  
344 database, regardless of the study area concerned, and the number of latent variables was  
345 determined following the rule of the first local minimum of the RMSECV, which varied  
346 between 2 and 9 (Table 6). The predictive capacities of the PLSR models ranged from low to  
347 medium to high, with RPD values of between 1.0 and 2.0 and with  $R^2_{cv}$  of between 0.02 and  
348 0.75 (Table 6). Three groups of variables can be identified from the cross-validation  
349 performance of the PLSR models (Table 6, Fig. 3): i) soil property models yielding  $R^2_{cv} \geq 0.5$   
350 and  $RPD \geq 1.4$  (rounded values) or models with intermediate to high levels of predictability;  
351 ii) soil property models with  $R^2_{cv}$  and RPD values of 0.4 and 1.3, respectively (rounded  
352 values) or models with poor predictive capacities just below thresholds commonly accepted in  
353 the literature or 'near intermediate' models; and iii) soil property models with  $R^2_{cv} < 0.4$  and  
354 RPD values of roughly 1 or models exhibiting poor or very poor levels of predictive capacity.

355 In overall, the Versailles Plain includes all 4 properties of group i (SOC, pH, CEC and  
 356 CaCO<sub>3</sub>) and one property of group ii (Clay), whereas the Peyne region includes 3 properties  
 357 of group ii (Clay, Iron and CEC), with the remaining properties (silt and sand content for both  
 358 regions and SOC, pH, and CaCO<sub>3</sub> content for the Peyne site) are categorized as group iii.

359

360

361

362

363

364

365 Table 6. Cross-validation performance statistics derived from the PLSR algorithm for soil  
 366 property prediction (NL<sub>v</sub>, number of latent variables; RMSE<sub>cv</sub> expressed in original units).

367 R<sup>2</sup><sub>cv</sub> and RPD rounded values of greater than or equal to 0.5 and 1.4, respectively, are shown  
 368 in bold (group *i*). RPD rounded values of greater than or equal to 1.3 are shown in italics  
 369 (group *ii*).

Soil property	Versailles Plain				Peyne Valley			
	R <sup>2</sup> <sub>cv</sub>	RMSE <sub>cv</sub>	RPD	NL <sub>v</sub>	R <sup>2</sup> <sub>cv</sub>	RMSE <sub>cv</sub>	RPD	NL <sub>v</sub>
SOC	<b>0.56</b>	1.23	<b>1.51</b>	4	0.02	3.71	1.00	4
CaCO <sub>3</sub>	<b>0.48</b>	20.3	<b>1.39</b>	4	0.15	122.2	1.08	8
Clay	<i>0.39</i>	1.23	<i>1.30</i>	6	<i>0.42</i>	56.4	<i>1.31</i>	5
Silt	0.14	103.0	1.09	3	0.11	91.9	1.06	9
Sand	0.22	81.7	1.14	4	0.03	113.0	1.02	7
Iron content	0.05	0.09	1.02	2	<i>0.45</i>	0.04	<i>1.34</i>	6
pH	<b>0.51</b>	0.51	<b>1.43</b>	4	0.08	0.64	1.03	4
CEC	<b>0.75</b>	1.23	<b>2.00</b>	6	<i>0.41</i>	2.41	<i>1.31</i>	6

370

371

372

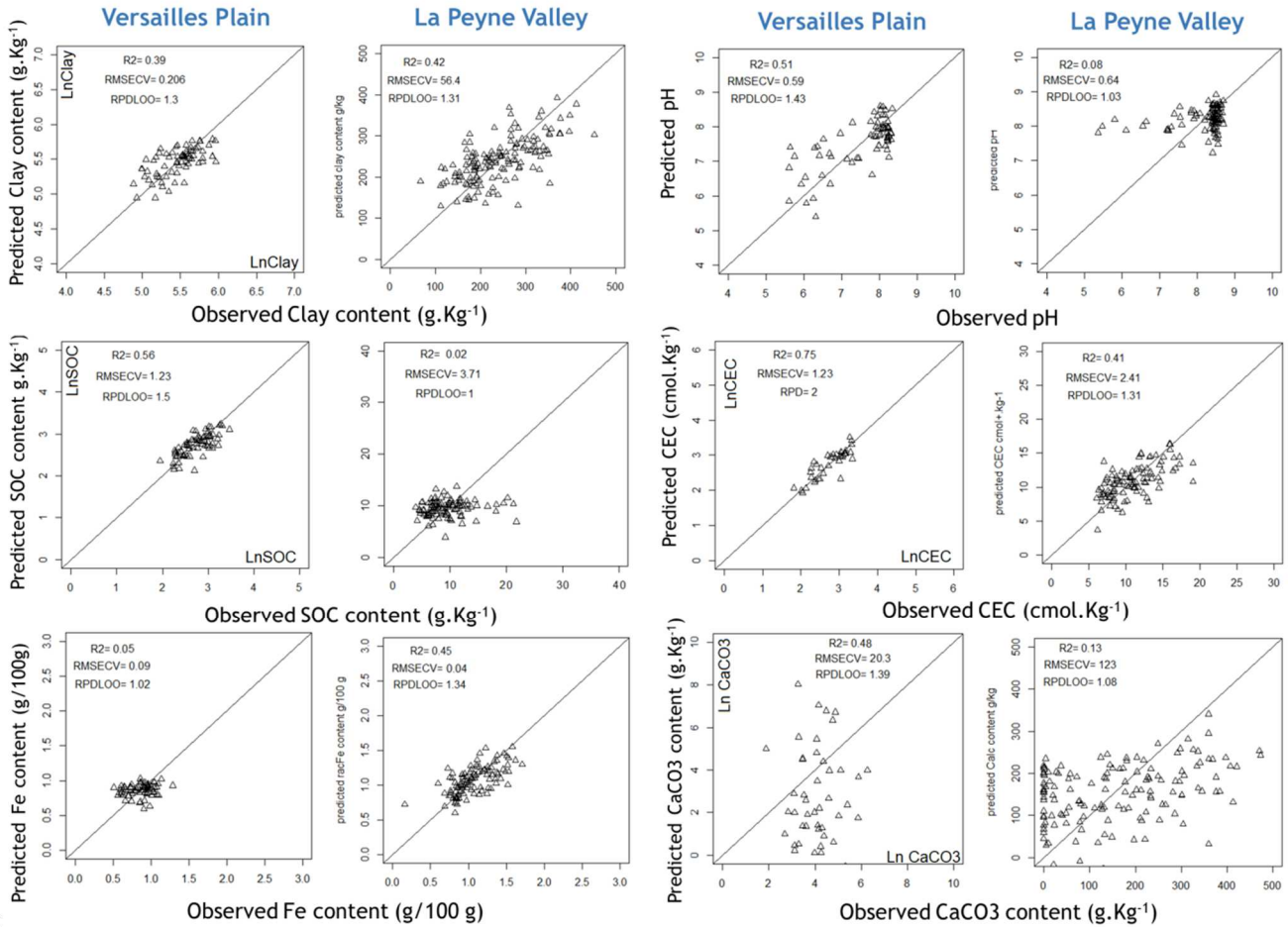
373

374

375

376

377



378

379 Figure 3. Predicted vs. observed soil properties for the Versailles Plain (left) and Peyne  
 380 Valley (right) for 6 soil properties best predicted for at least one region

381

382 A model property that exhibits intermediate or near intermediate predictive capacity for one  
 383 region can exhibit poor capacities for another. This is the case for pH, SOC, iron and CaCO<sub>3</sub>  
 384 content levels. A model property that exhibits high predictive capacity for one region can  
 385 exhibit near intermediate capacities for another: this is the case for CEC levels.

386

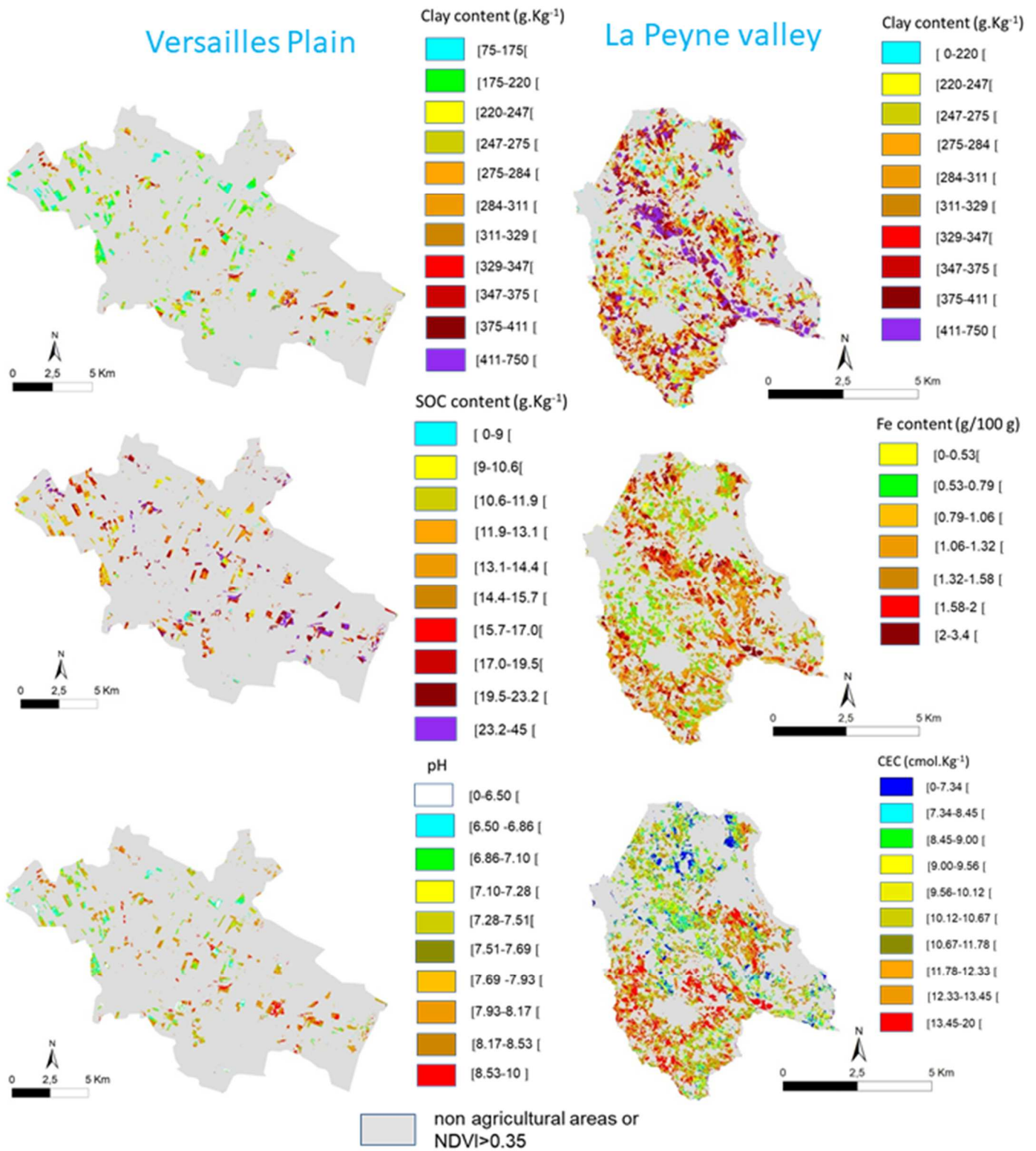
### 387 4.3 Soil property mapping from SENTINEL2 data

388 While retaining PLSR models for groups i and ii, equations were applied to bare cropland and  
 389 vineyard pixels (Fig. 4).

390 To relate the output maps to soil data and available soil maps and to facilitate the  
391 visual analysis of results for the other maps, and particularly for the Versailles Plain, for  
392 which the percentage of mapped pixels is very low, values were simplified to decile classes of  
393 predicted bare soil pixels for each study zone (Fig. 4).

394 The spatial patterns of clay correspond with known soil patterns for both regions. In  
395 the Peyne Valley, spatial patterns clearly show chromic luvisols developed along Plio-  
396 Quaternary alluvial terraces and characterized by high clay, iron and CEC levels. This result  
397 contrasts well with areas with Miocene marine deposits of calcisols and calcareous leptosols  
398 with less clay, iron and CEC. However, very high clay and iron content levels predicted for  
399 the minor riverbed of the Peyne River (the violet band in the clay map shown in Fig. 4) are  
400 not in accordance with our soil knowledge, likely revealing a perturbation related to soil  
401 moisture levels.

402 In the Versailles Plain, the highest predicted clay content levels match our  
403 observations of stagnic colluvic cambisols in lower slopes and valleys, whereas the lowest  
404 predicted clay content levels as expected were found along the plateaus with luvisols of loess  
405 origin. The highest SOC content levels were predicted both for stagnic colluvic cambisols in  
406 the valleys and for calcareous cambisols across the slopes, while low SOC content levels were  
407 predicted for luvisols originating from loess sources, in accordance with previous studies of  
408 the same region (Vaudour et al., 2013, 2016; Zaouche et al, 2017).



41

410 Figure 4. Maps of soil properties of the Versailles Plain (left) and Peyne Valley (right)

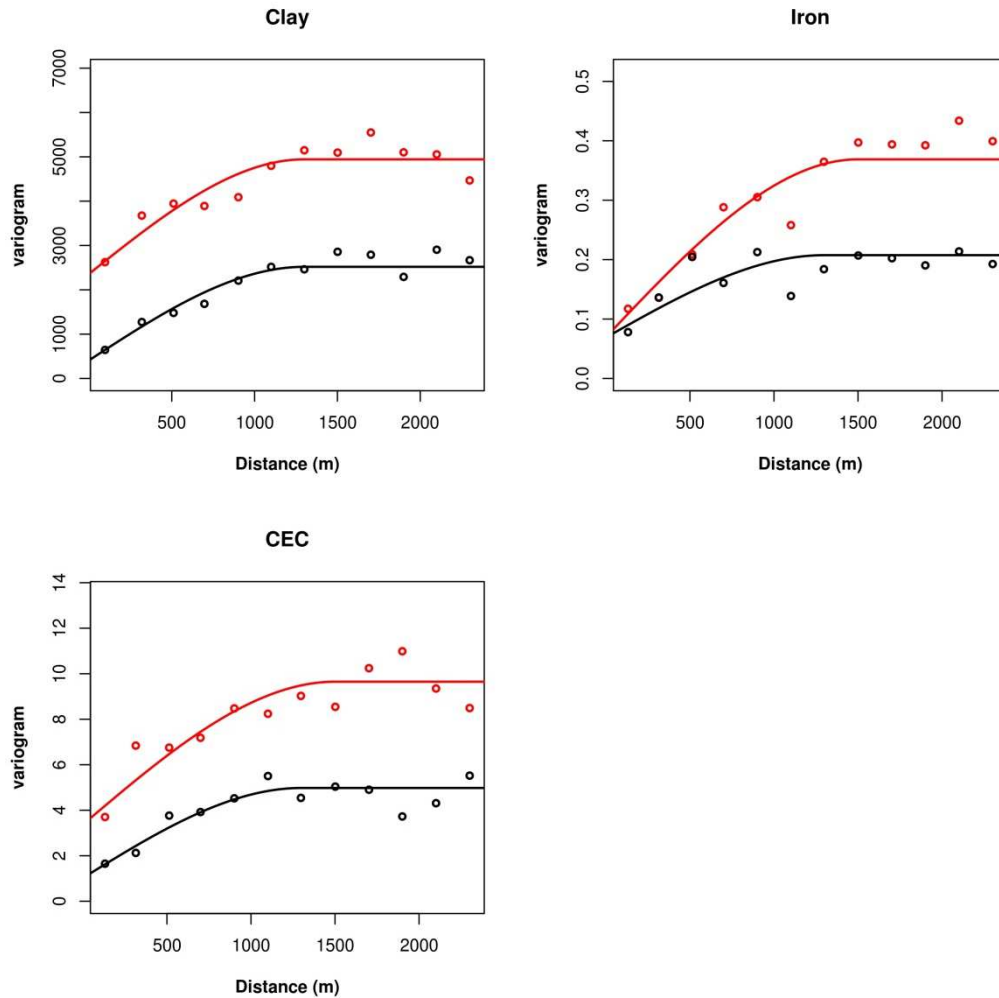
411

412

413 *4.4 S2A capacities to retrieve spatial structures*

414 *4.4.1 Comparisons between empirical variograms derived from measured and predicted*  
415 *values*

416 Following from the map examinations, comparisons drawn between variograms of predicted  
417 values of the three best predicted soil properties for the Payne Valley (clay, Fe, and CEC  
418 content, Fig. 5, black curves) and those of measured values for the same locations (Fig. 5 red  
419 curves) confirm that the soil patterns are captured by the predictions fairly well. Variograms  
420 for clay and CEC are very similar in shape and only show a decrease in the ‘nugget’ value (at  
421 the origin) of the predicted variogram. These differences in variograms have been observed  
422 through tests of soil predictions from hyperspectral data (Gomez et al, 2012). The predicted  
423 iron variogram has the same nugget and range as the measured one, with only a difference in  
424 ‘sill’ values (the slope of the variogram). No clear explanation can be given for this difference  
425 in behavior.



426

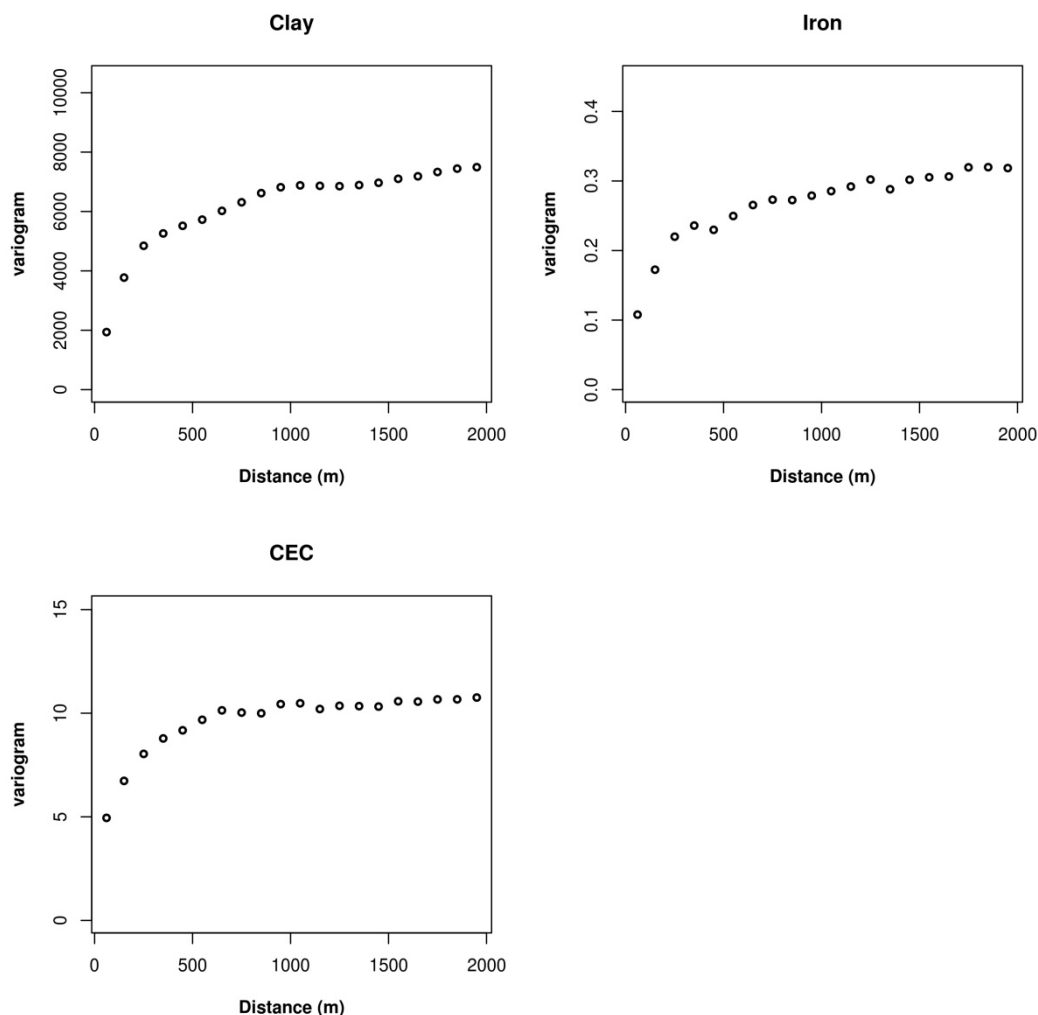
427 Figure 5. Empirical variograms calculated for clay, iron and CEC for the Payne Valley from  
 428 physico-chemical values of the collected soil samples (red points) and from predicted values  
 429 based on S2A spectra (black points) and fitted theoretical variograms (lines). Lag = 200 m.  
 430 Distance max: 2000 m.

431

432 *4.4.2 Spatial structures retrieved from the set of predicted pixels*

433 Empirical variograms were computed from the 46,971 pixels of bare soil in the Payne  
 434 catchment (Fig. 6). They exhibit different spatial structures from those revealed by  
 435 variograms built from the measured sites only (Fig. 5). From an increase in the number of  
 436 sites tested, short-scale variations are found across the clay and iron variograms as a result of  
 437 a first slope break at 250 m that is not shown in the previous variograms (Fig. 6). Another

438 slope break at approximately 1,000 m in the variograms shown in Fig. 6 is still visible but is  
439 less pronounced. This more complex spatial structure reveals a combination of soil variations  
440 acting at different scales in accordance with our understanding. The broad-scale variability  
441 found could be related to the spatial distribution of parent materials of soils with dissimilar  
442 clay and iron content levels. Short-range variations may result from erosion-redeposition  
443 processes occurring along slopes that involve neighboring parent materials with dissimilar  
444 iron and clay content levels.  
445



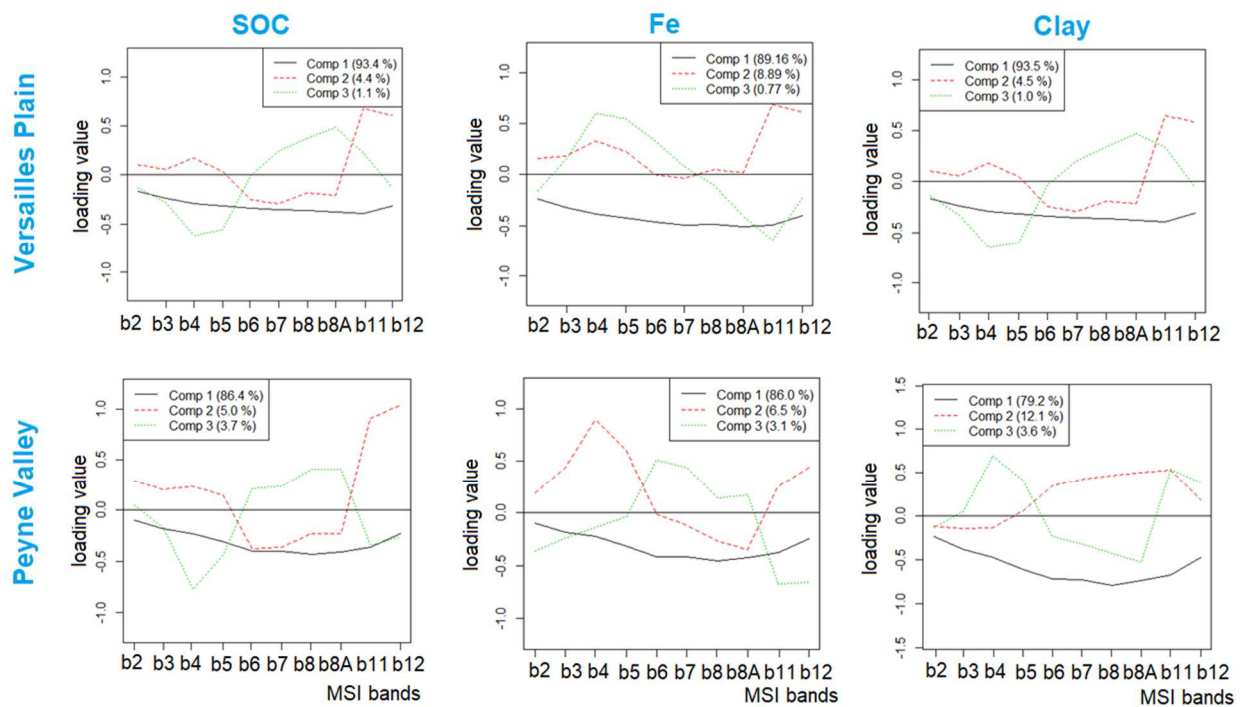
446  
447 Figure 6. Empirical variograms computed for clay, iron and CEC from predicted soil  
448 properties of bare soils of the Peyne. Lag = 100 m. Distance max: 2,000 m.

449

## 450 **5. Discussion**

### 451 *5.1 Performance of the S2A-derived PLSR models*

452 Comparisons of the performance of the S2A-derived models for two contrasting  
453 agroecosystems suggest that the predictability of a given property does not solely rely on the  
454 property itself or particularly on its spectral behavior as a “chromophore” according to Ben  
455 Dor et al. (2009). Rather, if such conditions could explain predictive capacities, both iron and  
456 SOC content levels would be predicted for any study area, as iron oxides and organic matter  
457 are spectrally influent due to their chemical compositions and arrangements, while their  
458 specific influent absorption bands are covered by MSI bands. In particular, SOC is known to  
459 be spectrally sensitive across the entire VNIR-SWIR spectral range (Ben Dor et al., 2009;  
460 Demattê et al., 2015), while the specific absorption wavelengths of iron oxides (550 nm and  
461 roughly 860-900 nm) are overlain by green band b3 and near-infrared band b8A. As was  
462 expected for SOC, loading values for SOC prediction models were found to be higher overall  
463 for the visible b4, b5, near infrared b8A and two SWIR bands (b11, b12) for the Versailles  
464 Plain than for the Peyne valley. For iron, loading values were found to be marked for the b3  
465 and b8A bands for the Peyne Valley while they were weakly expressed for the Versailles  
466 Plain (Fig. 7). This does not apply for both areas, suggesting that more conditions must be  
467 applied to confer predictive capacity. Moreover, clay predictions may be linked to the  
468 physical structure of soils in conjunction with a chromophore of approximately 2,200 nm that  
469 is fully covered by the b12 band (Table 1): this was revealed by higher loading values (Fig. 7)  
470 . However, performance of clay prediction was only found to be near-intermediate ( $0.5 > R^2_{cv}$   
471  $> 0.4$ ) for both study areas, suggesting that other conditions may hamper predictive capacity  
472 levels.



473

474 Figure 7. Loading plots for SOC, Fe and Clay of both study areas

475

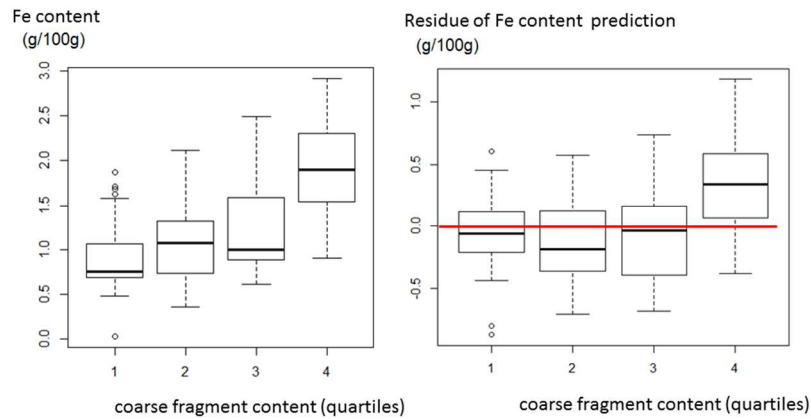
476 First, as previously found by Gomez et al. (2012) for the Payne Valley, intra-regional  
 477 variances between the considered properties are large unless considered variables (even when  
 478 spectrally sensitive) are not predictable. This is the case for both SOC and iron content levels,  
 479 which are neither abundant nor variable across the Payne Valley and Versailles Plain,  
 480 respectively.

481 Second, if the property considered is correlated with another well-predicted property,  
 482 this might improve its predictive ability. Performance levels obtained for pH (Versailles  
 483 Plain) and CEC (Versailles Plain, Payne Valley) are based on levels of variability across the  
 484 study regions and correlations to either SOC and/or clay. As a matter of fact, pH and CEC are  
 485 not spectrally sensitive. Moreover, while  $\text{CaCO}_3$  has a specific absorption band (2,330 nm),  
 486 its wavelength is not covered by any MSI band; its predictive ability might therefore be  
 487 attributed to its correlation to pH (0.6) for the Versailles Plain and other disturbing factors  
 488 might play a role for the Payne Valley. Although the prediction model for  $\text{CaCO}_3$  yielded

489 intermediate performance figures-of-merit (when rounded) for the Versailles Plain, a careful  
490 examination of the PLSR residues suggests that only soils with no or very low CaCO<sub>3</sub> content  
491 levels present low predictions errors (< 35 g.kg<sup>-1</sup>), and they represent 56% of the dataset,  
492 resulting in apparently average intermediate performance (Table 6). Specifically, calcareous  
493 soils of the Versailles Plain are as poorly predicted as those of the Peyne Valley. In addition,  
494 CaCO<sub>3</sub> degrades model accuracy levels for SOC content, as the lab uncertainty of SOC  
495 measurements increases with CaCO<sub>3</sub> content levels (Vaudour et al., 2016).

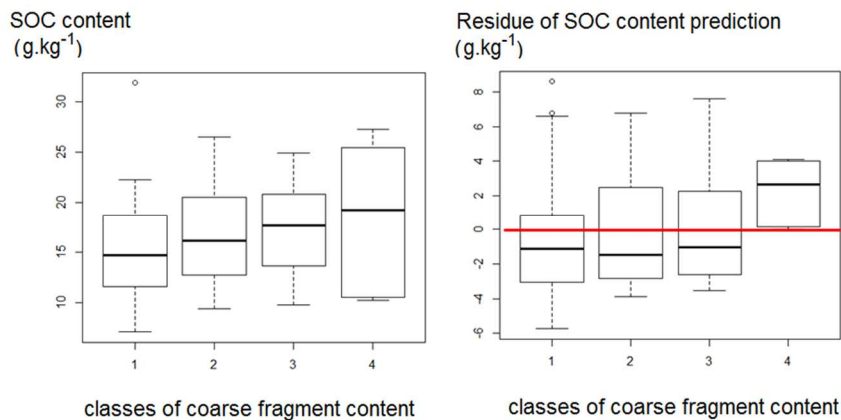
496 Third, the number and composition of sample sets is likely to influence prediction  
497 performance. For the Versailles Plain, strong performance recorded for CEC must be  
498 considered with caution, as it is based on a small sample size (39 samples) and the model may  
499 be overfit.

500 Fourth, soil surface conditions can be disturbed by soil roughness, soil moisture,  
501 emerging and non-covering vegetation, dry vegetation, vine stock and coarse fragment areal  
502 coverage. In addition to commonly known difficulties associated with PLSR models in terms  
503 of predicting high soil property values (e.g., for SOC (Stevens et al., 2012)), which are  
504 inherent to linear models, some additional disturbances can arise from these specific soil  
505 surface conditions. As a matter of fact, in the Peyne Valley, higher iron content levels are  
506 found among very stony soils with coarse fragment content levels of greater than 40%: the  
507 higher the coarse fragment content level, the more significant iron content prediction errors  
508 become (Fig. 8). In the Versailles Plain, because calcareous soils are stony and as their rock  
509 fragments are made of limestone, such relationships merge with those of calcium carbonate  
510 content: the higher the coarse fragment content level, the higher the CaCO<sub>3</sub> content level and  
511 the higher the SOC content level. The highest levels of CaCO<sub>3</sub> content (> 136 g. kg<sup>-1</sup>) show  
512 the highest levels of SOC residue prediction (Fig. 9).



513

514 Figure 8. Relationships between quartiles of coarse fragment content and Fe content (left) and  
 515 Fe content prediction errors (right) for the Payne Valley. Quartile thresholds of coarse  
 516 fragment content: 1, < 7.5%; 2, 7.5-18%; 3, 18-40%; 4, > 40%.



517

518 Figure 9. Relationships between quartiles of coarse fragment content and SOC content (left)  
 519 and effects of coarse fragment content on SOC content prediction errors (right) for the  
 520 Versailles Plain. Classes of coarse fragment content: 1, < 7.5%; 2, 7.5-18%; 3, 18-40%; 4, >  
 521 40%.

522

523 Of course, it cannot be inferred from Figs. 8 and 9 that coarse fragment content alone causes  
524 prediction errors, but presumably it contributes to such errors.

525 In terms of vegetation features, the composition and adequacy of the dataset is conditioned by  
526 the NDVI threshold. Regarding dry vegetation, while the b12 band covers the 2,100 nm  
527 specific absorption wavelength for cellulose (Daughtry 2001), the MSI bands do not enable  
528 one to derive an index of dry vegetation such as the Cellulose Absorption Index ( $CAI = 0.5$   
529  $(R_{2000\text{ nm}} + R_{2200\text{ nm}}) - R_{2100\text{ nm}}$ ) elaborated by Nagler et al. (2000). The CAI relies on two  
530 wavelengths covered by the b12 band (2,100 and 2,200 nm), but it requires the use of the  
531 2,000 nm wavelength not covered by any MSI band. However, other indexes, such as the  
532 Normalized Difference Tillage Index defined for Landsat Thematic Mapper (TM) bands  
533 ( $NDTI = (TM5 - TM7) / (TM5 + TM7)$ ) (Van Deventer et al., 1997), could be adapted and tested  
534 for discriminating crop residue cover. The S2A data thus show limits in accounting for crop  
535 residue cover and vine wood vegetation more than the MSI spatial resolution does not enable  
536 one to discriminate between vine rows and vine interrows to remove the spectral influence of  
537 vine woods.

538

539 In conclusion, our use of two contrasting agroecosystems datasets denotes what is achievable  
540 from S2A data in terms of predictive capacities for a single considered date. The soils  
541 considered in this study are located in French regions but widely develop abroad, across the  
542 temperate and Mediterranean areas. Assessment of Sentinel-2 performance is developing for  
543 other French regions with other soil types and further for tropical soils.

544

545

546

547

548 *5.2 Comparisons with other sensors*

549 Our model performs in a similar manner as those employed in other studies. It  
550 performs better than SPOT multispectral satellite images in measuring SOC, and it performs  
551 similarly or less optimally than hyperspectral airborne images in measuring all properties.

552 For the Versailles Plain in particular, previous models of SOC content were derived  
553 from multispectral or hyperspectral fields or from image spectra. In terms of RMSECV and  
554 RPD values in particular, the regional PLSR model obtained SOC content levels from S2A  
555 spectra (1.23 g.kg<sup>-1</sup> and 1.51, respectively) more accurately than real SPOT or simulated  
556 SPOT spectra (Vaudour et al., 2013: error range 4.5-6.0 g.kg<sup>-1</sup>, RPD 0.9-1.3) for the same  
557 region. This is presumably attributable to the beneficial role of its SWIR bands and to  
558 differences in soil surface conditions, which are similar to those obtained from a VNIR  
559 hyperspectral AISA airborne image (no SWIR) for the same region (Vaudour et al., 2016:  
560 error range 2.82-3.79 g.kg<sup>-1</sup>, RPD 1.3-1.6).

561 For the Peyne Valley, performance outcomes obtained from Sentinel-2 are lower  
562 than those obtained from a VNIR-SWIR Hymap airborne image (Gomez et al., 2012),  
563 regardless of soil properties involved with dramatic changes in performance found for CaCO<sub>3</sub>  
564 content effectively predicted from the hyperspectral spectra but not predicted from S2A  
565 spectra (see §5.1). However, due to intra-regional variances (SOC) and an absence of  
566 correlations with more effectively predicted properties (silt), neither SOC nor silt content  
567 levels were predicted from hyperspectral and S2A images. Performance degradation from  
568 airborne to spaceborne models has also been found by Steinberg et al. (2016) for SOC, clay  
569 and iron content levels, though these authors used simulated EnMAP satellite spectra.

570 It must be noted that our models were constructed from actual spaceborne images that  
571 account for the effects of atmospheric, signal/noise ratio, and soil surface conditions and

572 notably coarse fragment content and vegetation. This distinguishes our models from those  
573 constructed from simulated MSI spectra derived from lab spectral libraries, as anticipated by  
574 Castaldi et al. (2016) for a number of forthcoming or newly launched satellites, including  
575 Sentinel-2. However, with the addition of noise and atmospheric effects and from the use of  
576 untransformed lab reflectance spectra sampled from central and southern Italy, these authors  
577 obtained validation results similar to our performance results for clay ( $R^2$  0.36-0.42; RPD  
578 1.26-1.35) that are inferior to those found for the Versailles Plain in terms of SOC content  
579 levels ( $R^2$  0.36; RPD 1.26) in the best case or that are not as predictive as found for the Payne  
580 ( $R^2$  0.13; RPD 1.09) in the worst case. Gomez et al. (2018) used VNIR/SWIR hyperspectral  
581 airborne data (initial spectral resolution of approximately 5 nm) to simulate, among others,  
582 Sentinel-2, Landsat 8 and Landsat 7 spectral resolution data. They showed that these  
583 multispectral sensors provide very modest performances of clay content estimations, as these  
584 spectral resolutions do not provide clay absorption feature useful in regression models.

585

### 586 *5.3 Maximizing the mapped area*

587 As the presence of vegetation severely hampers the prediction of soil properties from  
588 VNIR/SWIR remote sensing data, it is important to retrieve as many bare soil signals as  
589 possible. When only one image is considered, as was done in this study, this involves a  
590 careful selection of acquisition periods. Images of the Versailles Plain and Payne Valley were  
591 acquired for the spring period to maximize the size of the area with bare soils. In temperate  
592 agroecosystems like that of the Versailles Plain, this corresponds to the sowing of spring  
593 cereals, with the winter period being less suitable due to impacts of the Nitrate Directive that  
594 requires intermediate crop cultivation (Vaudour et al., 2013). In a Mediterranean  
595 agroecosystem like that of the Payne Valley, the spring period corresponds to maximum tilled  
596 vineyard coverage for removing weeds (Paré, 2007) while green vegetation is not yet present.

597 Despite this careful selection of periods, coverage levels found for bare soil areas remain  
598 modest, especially for the Versailles Plain (Fig. 4).

599 Bare soil areas could be maximized (at least for temperate agroecosystems) by  
600 aggregating multiple acquisition dates. This would allow one to accumulate the spectra of soil  
601 areas that change every year and along the crop cycle. Sentinel-2 is particularly well suited to  
602 this task, as it provides an image every 5 days, thus increasing the likelihood of acquiring  
603 images under clear conditions and across the crop rotation cycle.

604 Such an aggregation of images for maximizing bare soil areas was already attempted  
605 by Diek et al. (2016). These authors doubled the bare soil area by combining hyperspectral  
606 APEX acquisitions over 3 successive years and performed intercalibration from linear  
607 regressions of atmospherically corrected spectra for different years. This raises issues relating  
608 to accurate atmospheric corrections across dates and to the number and anteriority values of  
609 dates. This issue is being studied in reference to the Versailles Plain to consider the  
610 directional effects of soil roughness in line with tillage operations (Vaudour et al., 2014a).  
611 Indeed, soil roughness levels can be spatially and temporally retrieved from optical/radar  
612 pairs such as S2/S1 (Vaudour et al., 2014b), which could be accounted for during soil  
613 properties prediction.

614 Bare soil coverage levels can also be increased by applying unmixing techniques that  
615 isolate bare soil signals from semi-vegetated pixels (Bartholomeus et al 2011, Ouerghemmi et  
616 al., 2016). For the Peyne Valley, such techniques are used to predict clay content levels from  
617 hyperspectral data for semi-vegetated areas ( $NDVI < 0.55$ ), expanding the studied surface  
618 from 4% (bare soil) to 63% of the total area (Ouerghemmi et al., 2016). A similar approach  
619 could be applied for S2A soil predictions.

620

621

622

623 *5.4. Incorporating S2A data into the framework of digital soil mapping*

624 The soil predictions obtained from S2A are neither precise nor extended enough to be  
625 exploited “as is” by end users. They must rather be considered as a new source of soil data  
626 that should be used for Digital Soil Mapping (Mc Bratney et al, 2003, Lagacherie et al, 2007),  
627 a larger methodological framework that can produce more exhaustive and precise soil maps.

628 If we examine the soil property predictions obtained in this study with such a perspective in  
629 mind, S2A soil predictions obtained from this study could serve as valuable inputs for digital  
630 soil mapping for two reasons.

631 First, S2A data offer insight on the spatial patterns of certain soil properties that could be  
632 quantified from variograms that closely resemble those obtained from real measurements.  
633 These variograms could be used to optimize further sampling efforts, as they allow one to  
634 compute error variances (kriging variance) for sampling schemes of different densities and  
635 spatial distributions and thus determine the sampling efforts required to meet target levels of  
636 precision in spatial predictions (McBratney et al., 1981).

637 Second, S2A products could serve as surrogate data to improve the precision of Digital Soil  
638 Mapping models (Lagacherie & Gomez; 2013). For example, Walker et al. (2017) found the  
639 use of hyperspectral data as soft data for co-kriging or cokriging with external drift models to  
640 improve prediction performance. Although less pronounced, improvements were still  
641 observable when using hyperspectral-based estimations of moderate quality ( $R^2 < 0.5$ ) like  
642 many of those obtained in this study. It is therefore expected that some S2A soil outputs could  
643 make improvements while being more available than hyperspectral data.

644 Finally, the potential of S2 data as a co-variable in DSM model could further be evaluated.  
645 While previous researches used MODIS or LANDSAT data in DSM models, either as  
646 spectral indexes, such as the NDVI (e.g., Mishra et al., 2010), or as spectral bands (e.g., Were

647 et al., 2015). Zaouche et al (2018) found improvement incorporating the green band of SPOT  
648 into a joint Bayesian model, and development of their approach is in progress for Sentinel2.

649

## 650 **6. Conclusion**

651 S2A image spectra acquired from two French study areas representative of temperate and  
652 Mediterranean agroecosystems—the Versailles Plain and the Payne Valley—were tested as  
653 input data of a chemometric model (PLSR) to predict 8 topsoil properties of bare soil areas:  
654 8% and 39% of the Versailles Plain and the Payne Valley, respectively. Six of these 8 soil  
655 properties (clay, SOC, iron, CaCO<sub>3</sub>, pH, and CEC levels) can be predicted with varying  
656 success depending on their intrinsic spectral properties, intra-regional variances, correlations  
657 and soil surface conditions. Some of the best predictions were also found to serve as good  
658 approximations of the spatial patterns of soil properties.

659 Although a significant decline in the prediction performance of those obtained from  
660 hyperspectral data for the same study areas was observed, S2A soil predictions can serve as  
661 valuable inputs for Digital Soil Mapping. With the current absence of efficient hyperspectral  
662 satellites that can deliver hyperspectral data, it is advantageous to allow for the mosaicking of  
663 multirate acquisition and for the selection of the best acquisitions over a time series. We  
664 therefore recommend their use to improve the performance of Digital Soil mapping  
665 predictions.

666

## 667 **Acknowledgment**

668 This study was carried out in the framework of the TOSCA “Cartographie Numérique des  
669 Sols (CNS)” program of the French Space Agency (CNES). It also benefited support from the  
670 TOSCA-PLEIADES-CO program of the CNES for the Versailles Plain. Special thanks to  
671 Dalila Hadjar, Arthur Scriban, Paulina Michura, for technical assistance in the field. We are

672 also indebted to Yves Blanca, IRD-UMR LISAH Montpellier, for the soil samples sampling  
673 in 2009 over the vineyard Plain of Languedoc.

674

675 **References**

676 AFNOR, 1999. Qualité des sols. AFNOR, Paris, vol. 1, 565 p. (in French)

677 Adeline K., Gomez C., Gorretta N., Roger J.M., 2017. Predictive ability of soil properties to  
678 spectral degradation from laboratory Vis-NIR spectroscopy data. *Geoderma*. 288, pp.  
679 143–153.

680 Adhikari, K., Hartemink, A.E., 2016. Linking soils to ecosystem services - a global review.  
681 *Geoderma* 262, 101–111.

682 Arrouays, D., Grundy, M.G., Hartemink, A.E., Hempel, J.W., Heuvelink, G.B.M., Young  
683 Hong, S., Lagacherie, P., Lelyk, G., McBratney, A.B., McKenzie, N.J., Mendonça-  
684 Santos, M.L., Minasny, B., Montanarella, L., Odeh, I.O.A., Sanchez, P.A., Thompson,  
685 J.A., Zhang, G.L., 2014. GlobalSoilMap: toward a fine-resolution global grid of soil  
686 properties. *Advances in Agronomy*, 125, 93-134.

687 Arrouays, D., Lagacherie, P., Hartemink, A.E., 2017. Digital soil mapping across the globe.  
688 *Geoderma Reg.* 9, 1–4.

689 Bartholomeus, H., Kooistra, L., Stevens, A., Leeuwen, M., Wesemael, B., Ben-Dor, E.,  
690 Tychon, B., 2011. Soil organic carbon mapping of partially vegetated agricultural fields  
691 with imaging spectroscopy. *International Journal of Applied Earth Observation and*  
692 *Geoinformation* 13 (1), 81–88.

693 Baveye, P., Baveye, J., Gowdy, J., 2016. Soil “ecosystem” services and natural capital:  
694 critical appraisal of research on uncertain ground. *Frontiers in Environmental Science*, 4  
695 (41).

696 Ben-Dor, E., Chabrillat, S., Demattê, J.A.M., Taylor, G.R., Hill, J., Whiting, M.L., Sommer,  
697 S., 2009. Using imaging spectroscopy to study soil properties. *Remote Sens. Environ.*  
698 113, S38-S55.

699 Castaldi, F., Palombo, A., Santini, S., Pignatti, S., Casa, R., 2016. Evaluation of the potential  
700 of the current and forthcoming multispectral and hyperspectral imagers to estimate soil  
701 texture and organic carbon. *Remote Sensing of Environment*, 179, 54-65.

702 Chang, C.W., Laird, D.A., Mausbach, M.J., Hurburgh, C.R., 2001. Near infrared reflectance  
703 spectroscopy: principal components regression analysis of soil properties. *Soil Sci. Soc.*  
704 *Am. J.* 65, 480-490.

705 Crahet, M., 1992. Soil Map of the Versailles Plain. Scale 1:50 000. Institut National  
706 Agronomique Paris-Grignon, Grignon, Internal report.

707 Daughtry, C.S.T., 2001. Discriminating crop residues from soil by shortwave infrared  
708 reflectance. *Agron. J.* 93, 125-131.

709 Demattê, J., Morgan, C.L.S. Chabrillat, S., Rizzo, R., Franceschini, M.H.D., Terra, F.daS.,  
710 Vasques, G.M., Wetterlind J., 2015. Spectral sensing from ground to space in soil  
711 science: State of the art, applications, potential and perspectives. In book: *Remote*  
712 *Sensing Handbook - Land Resources Monitoring, Modeling, and Mapping with Remote*  
713 *Sensing*, Publisher: CRC Press, Editors: P.S. Thenkabail, pp.661-732.

714 Diek, S., Schaepman, M.E., de Jong, R., 2016. Creating Multi-Temporal Composites of  
715 Airborne Imaging Spectroscopy Data in Support of Digital Soil Mapping. *Remote Sens.*  
716 8, 906.

717 Filzmoser, P., Garrett, R.G., Reimann, C., 2005. Multivariate outlier detection in exploration  
718 geochemistry. *Computers&Geosciences* 31, 579-587.

719 Folkman, M., Pearlman, J., Liao, L., Jarecke, P., 2001. EO1/Hyperion hyperspectral imager  
720 design, development, characterization and prediction. In: Smith, W.L., Yasuoka, Y.  
721 (Eds.), *Hyperspectral Remote Sensing of the Land and Atmosphere*. SPIE Proceeding,  
722 vol. 4151, pp. 40–51.

723 Geladi, P., Kowalski, B. R., 1986. Partial least squares regression: a tutorial. *Analytica*  
724 *Chimica Acta* 185, 1-17.

725 Gomez, C., Adeline, K., Bacha, S., Driessen, B., Gorretta, N, Lagacherie, P, Roger, JM,  
726 Briottet, X., 2018. Sensitivity of clay content prediction to spectral configuration of  
727 VNIR/SWIR imaging data, from multispectral to hyperspectral scenarios. *Remote*  
728 *Sensing of Environment* 204, 18-30.

729 Gomez, C., Viscarra Rossel, R.A., McBratney, A.B., 2008. Soil organic carbon prediction by  
730 hyperspectral remote sensing and field vis-NIR spectroscopy: an Australian case study.  
731 *Geoderma* 146, 403–411.

732 Gomez, C., Coulouma, G., Lagacherie, P., 2012a. Regional predictions of eight common soil  
733 properties and their spatial structures from hyperspectral Vis–NIR data, *Geoderma*,  
734 189–190, 176-185.

735 Gomez, C., Lagacherie P., Bacha, S., 2012b. Using an VNIR/SWIR hyperspectral image to  
736 map topsoil properties over bare soil surfaces in the Cap Bon region (Tunisia). In  
737 “Digital Soil Assessments and Beyond” Minasny B., Malone B.P., McBratney A.B.  
738 (Ed.). Springer, 387-392.

739 Gomez, C., Oltra-Carrió, R., Bacha, S., Lagacherie, P., Briottet, X., 2015. Evaluating the  
740 sensitivity of clay content prediction to atmospheric effects and degradation of image  
741 spatial resolution using hyperspectral VNIR/SWIR imagery. *Remote Sens. Environ.*  
742 164, 1-15.

743 Goovaerts, P., 1997. Geostatistics for natural resources evaluation. Oxford University Press,  
744 New York.

745 Hagolle, O., 2013. Séries temporelles, SPOT4 Take Five blog, URL: <http://www.cesbio.upstlse.fr/multitemp/>  
746

747 Hagolle, O., Huc, M., Villa Pascual, D., Dedieu, G., 2010. A multi-temporal method for cloud  
748 detection, applied to FORMOSAT-2, VEN $\mu$ S, LANDSAT and SENTINEL-2 images.  
749 Remote Sens. Environ. 114, 1747-1755.

750 Kennard R. W., Stone L. A., 1969. Computer aided design of experiments. Technometrics 11,  
751 1, 137–148.

752 Lagacherie, P., Sneep, A.-R., Gomez, C., Bacha, S., Coulouma, G., Hamrouni, M.H., Mekki,  
753 I., 2013. Combining Vis–NIR hyperspectral imagery and legacy measured soil profiles  
754 to map subsurface soil properties in a Mediterranean area (Cap-Bon, Tunisia).  
755 Geoderma 209–210, 168–176.

756 Mark, H.L., Tunnell, D., 1985. Qualitative near-infrared reflectance analysis using  
757 Mahalanobis distances. Anal. Chem. 57, 1449-1456.

758 McBratney, A. B., Webster, R., Burgess, T. M.: The design of optimal sampling schemes for  
759 local estimation and mapping of regionalized variables. I. Theory and Method,  
760 Computers and Geosciences, 7, 331–334, 1981.

761 McBratney, A.B., Mendonca Santos, M.L., Minasny, B., 2003. On digital soil mapping.  
762 Geoderma 117, 3–52.

763 Mehra O.P., Jackson M.L., 1960. Iron oxide removal from soils and clays by a dithionite-  
764 citrate system buffered with sodium bicarbonate. In Clays and Clay Minerals;  
765 Proceedings of the 7th Conference, Natl Acad. Sci-Natl Res. Council Publ.,  
766 Washington, DC, pp. 317-327.

767 Mevik B.H., Wehrens R., 2007. The pls package: principal component and partial least  
768 squares regression in R. *Journal of Statistical Software* 18, 2, 1-24.

769 Minasny, B., McBratney, A.B., 2016. Digital soil mapping: A brief history and some lessons.  
770 *Geoderma* 264, 301–311.

771 Nagler, P.L., Daughtry, C.S.T., Goward, S.N., 2000. Plant litter and soil reflectance. *Remote*  
772 *Sens. Environ.* 71, 207-215.

773 Mishra, U., Lal, R., Liu, D., Van Meirvenne, M., 2010. Predicting the Spatial Variation of the  
774 Soil Organic Carbon Pool at a Regional Scale. *Soil Science Society of America Journal*  
775 74, 906. <https://doi.org/10.2136/sssaj2009.0158>

776 Ouerghemmi, W., Gomez, C., Naceur, S., Lagacherie, P., 2016. Semi-blind source separation  
777 for the estimation of the clay content over semi-vegetated areas using VNIR/SWIR  
778 hyperspectral airborne data. *Remote Sens. Environ.* 181, 251–263.

779 Paré, N., 2007. Etude de la variabilité et de la dynamique des états de surface des sols  
780 viticoles méditerranéens. Master Thesis AgroParisTech Paris.

781 Pebesma, E.J., 2004. Multivariable geostatistics in S: the gstat package. *Comput. Geosci.* 30,  
782 683–691.

783 R Development Core Team, 2015. The Comprehensive R Archive Network. The R  
784 Foundation for Statistical Computing, Wirtschaft Universitat, Vienna, Austria. URL:  
785 <http://www.r-project.org/>

786 Ramirez-Lopez, L., Schmidt, K., Behrens, T., Van Wesemael, B., Demattê, J.A.M., Scholten,  
787 T., 2014. Sampling optimal calibration sets in soil infrared spectroscopy. *Geoderma*  
788 226-227, 140-150.

789 Richter, R., Schläpfer, D., 2016. ATCOR2/3 User guide, v.9.0.2, March 2016, 263 p.

790 Sanchez, P.A., Ahamed, S., Carré, F., Hartemink, A.E., Hempel, J., Huising, J., Lagacherie,  
791 P., McBratney, A.B., McKenzie, N.J., Mendonca Santos, M.L., Minasny, B.,  
792 Montanarella, L., Okoth, P., Palm, C.A., Sachs, J.D., Shepherd, K.D., Vågen, T.-G.,  
793 Vanlauwe, B., Walsh, M.G., Winowiecki, L.A., Zhang, G.-L., 2009. Environmental  
794 science. Digital soil map of the world. *Science* 325, 680–1.

795 Selige, T., Böhner, J., Schmidhalter, U., 2006. High resolution topsoil mapping using  
796 hyperspectral image and field data in multivariate regression modeling procedures.  
797 *Geoderma* 136, 235–244. <https://doi.org/10.1016/j.geoderma.2006.03.050>

798 Shabou, M., Mougenot, B., Chabaane, Z.L., Walter, C., Boulet, G., Aissa, N.B. Zribi, M.  
799 2015. Soil Clay Content Mapping Using a Time Series of Landsat TM Data in Semi-  
800 Arid Lands. *Remote Sensing*. 7, 6059-6078.

801 Steinberg, A., Chabrillat, S., Stevens, A., Segl, K., Foerster, S., 2016. Prediction of common  
802 surface soil properties based on Vis-NIR airborne and simulated EnMAP imaging  
803 spectroscopy data: prediction accuracy and influence of spatial resolution. *Remote*  
804 *Sensing*, 8, 613. Doi:10.3390/rs8070613

805 Stevens, A., Miralles, I., Van Wesemael, B., 2012. Soil organic carbon predictions by  
806 airborne imaging spectroscopy: comparing cross-validation and validation. *Soil Sci.*  
807 *Soc. Am. J.* 76, 2174-2183.

808 Stevens, A., Udelhoeven, T., Denis, A., Tychon, B., Liroy, R., Hoffman, L., Van Wesemael,  
809 B., 2010. Measuring soil organic carbon in croplands at regional scale using airborne  
810 imaging spectroscopy. *Geoderma* 158, 32-45.

811 Van Deventer, A.P., Ward, A.D., Gowda, P.H., Lyon, J.G., 1997. Using Thematic Mapper  
812 data to identify contrasting soil plains and tillage practices. *Photogrammetric*  
813 *Engineering & Remote Sensing* 63, 1, 87-93.

814 Vaudour, E., Bel, L., Gilliot, J.M., Coquet, Y., Hadjar, D., Cambier, P., Michelin, J., Houot,  
815 S., 2013. Potential of SPOT multispectral satellite images for mapping topsoil organic  
816 carbon content over peri-urban croplands. *Soil Sci. Soc. Am. J.* 77, 2122-2139.

817 Vaudour, E., Gilliot, J.M., Bel, L., Bréchet, L., Hadjar, D., Hamiache, J., Lemonnier, Y.,  
818 2014a. Uncertainty of soil reflectance retrieval from SPOT and RapidEye multispectral  
819 satellite images using a per-pixel bootstrapped empirical line atmospheric correction  
820 over an agricultural region. *International Journal of Applied Earth Observation and*  
821 *Geoinformation* 26, 217-234.

822 Vaudour, E., Baghdadi, N., Gilliot, J.M., 2014b. Mapping tillage operations over a peri-urban  
823 region using combined SPOT4 and ASAR/ENVISAT images. *Int. J. Appl. Earth*  
824 *Observ.Geoinf.* 28, 43-59.

825 Vaudour, E., Gilliot, J.M., Bel, L., Lefevre, J., Chehdi, K., 2016. Regional prediction of soil  
826 organic carbon content over temperate croplands using visible near-infrared airborne  
827 hyperspectral imagery and synchronous field spectra. *Int. J. Appl. Earth Observ.Geoinf.*  
828 49, 24-38.

829 Vaudour, E., Noirot-Cosson, P.E., Membrive, O., 2015. Early-season mapping of crops and  
830 cultural operations using very high spatial resolution Pléiades images. *Int. J. Appl. Earth*  
831 *Observ.Geoinf.* 42, 128-141.

832 Wold, S., Sjöström, M., Eriksson, L., 2001. PLS-regression: a basic tool of chemometrics.  
833 *Chemometrics and Intelligent Laboratory Systems* 58, 109-130.

834 World Reference Base (WRB), 2014. World reference base for soil resources. A framework  
835 for international classification, correlation and communication. Food and Agriculture  
836 Organization of the United Nations, Rome, 128 p.

837 Zaouche, M., Bel, L., Vaudour, E., 2017. Geostatistical mapping of topsoil organic carbon  
838 and uncertainty assessment in Western Paris croplands (France). *Geoderma Regional*  
839 10, 126-137.

840 Were, K., Bui, D.T., Dick, Ø.B., Singh, B.R., 2015. A comparative assessment of support  
841 vector regression, artificial neural networks, and random forests for predicting and  
842 mapping soil organic carbon stocks across an Afromontane landscape. *Ecological*  
843 *Indicators* 52, 394–403. <https://doi.org/10.1016/j.ecolind.2014.12.028>

844 Zaouche, M., Bel, L., Tressou, J., Vaudour, E., 2018. Soil organic carbon modelling using  
845 jointly different sources. METMA2018, Montpellier (France), poster.  
846 <http://metma2018.sfds.asso.fr/assets/Download/proceedingsMETMA9.pdf>

#### 847 **List of figure captions**

848 Figure 1. Locations of soil samples from the Versailles Plain (left, infrared colored S2A  
849 image from 12 March 2016) and the lower Peyne Valley (right, infrared colored S2A image  
850 from 19 March 2016), ©ESA 2016

851 Figure 2. Selection of reflectance image spectra covering the whole dataset reflectance range  
852 and the main soil types

853 Figure 3. Predicted vs. observed soil properties for the Versailles Plain (left) and Peyne  
854 Valley (right) for 6 soil properties best predicted for at least one region

855 Figure 4. Maps of soil properties of the Versailles Plain (left) and Peyne Valley (right)

856 Figure 5. Empirical variograms calculated for clay, iron and CEC for the Peyne Valley from  
857 physico-chemical values of the collected soil samples (red points) and from predicted values  
858 based on S2A spectra (black points) and fitted theoretical variograms (lines). Lag = 200 m.  
859 Distance max: 2000 m.

860 Figure 6. Empirical variograms computed for clay, iron and CEC from predicted soil  
861 properties of bare soils of the Peyne. Lag = 100 m. Distance max: 2,000 m.

862 Figure 7. Loading plots for SOC, Fe and Clay of both study areas

863 Figure 8. Relationships between quartiles of coarse fragment content and Fe content (left) and

864 Fe content prediction errors (right) for the Peyne Valley. Quartile thresholds of coarse

865 fragment content: 1, < 7.5%; 2, 7.5-18%; 3, 18-40%; 4, > 40%.

866 Figure 9. Relationships between quartiles of coarse fragment content and SOC content (left)

867 and effects of coarse fragment content on SOC content prediction errors (right) for the

868 Versailles Plain. Classes of coarse fragment content: 1, < 7.5%; 2, 7.5-18%; 3, 18-40%; 4, >

869 40%.

870